Seismic Performance of Precast Bridge Columns with Socket and Pocket Connections Based on Quasi-Static Cyclic Tests: Experimental and Numerical Study

Zhiqiang Wang[1]; Tiantian Li[2]; Hongya Qu[3]; Hongyi Wei[4]; and Yongbo Li[5]

Abstract: In this study, four 1/3-scale bridge column specimens were investigated both experimentally and numerically. The specimens consisted of two cast-in-place (CIP) reference columns and two precast columns for the study of socket and pocket connections, respectively. The precast columns were designed based on the actual application of precast urban viaducts in Shanghai, China. Therefore, this study investigated and verified the seismic performance of these connection approaches. Based on the test results of the hysteretic behavior and derived indexes, both columns with socket and pocket connections have shown equivalent seismic performances to their CIP references. The differences between precast and CIP columns were within 15% for all indexes, and the damage development and failure mechanism were also similar. Finite-element models were created with displacement analyser (DIANA) and calibrated with the test data. Bond-slip behavior with the built-in embedded reinforcement element, concrete cracking with tension softening, and material nonlinearity were considered. Under monotonic pushover analysis, the load-displacement curves were in good agreement with the backbone curves of the test results. **DOI: 10.1061/(ASCE)BE.1943-5592.0001463.**

Author keywords: Bridge column; Cyclic loading; Finite-element method; Pocket connection; Socket connection; Precast concrete; Seismic performance.

Introduction

Recent advancements in precast bridge design and construction have resulted in faster construction speed, less traffic interruption, better structural robustness, less environmental impact, and lower cost (Bu et al. 2016). Four different types of connections (bar couplers, grouted ducts, pocket connections, and member socket connections) have been studied and applied in practical applications (Raynor et al. 2002; Ichinose et al. 2004; Ou 2007; Steuck et al. 2009; Zhou et al. 2010; Marsh et al. 2011; Murcia-Delso et al. 2013; Brunesi et al. 2015), while the performance of the precast bridges in middle- to high-seismic regions still needs to be further studied due to the limited understanding. Therefore, it is necessary to investigate the existing precast bridges in these regions to confidently verify the engineering feasibility. This study focused on the seismic behaviors of the socket and pocket connections that have been applied to real bridge structures, and therefore only state-of-the-art investigations of direct relevance were reviewed.

Pocket connections were originally designed to connect columns to cap beams. They leave a large opening, or pocket, in a member of the bridge substructure (e.g., cap beam or footing). The projecting reinforcement from another member (column) is inserted into the pocket. The pocket is then filled with cast-in-place (CIP) concrete. The casting process of the pocket typically takes more time than other types of connections, but it allows more installation tolerance as long as the joint region is not heavily reinforced (Marsh et al. 2011). Matsumoto (2009) conducted an experimental study of two precast column-to-cap joints with the pocket connection, and they were tested to compare with the CIP reference specimen. It was found that the precast specimens were of equivalent strength and ductility to the CIP reference. Restrepo et al. (2011) studied the seismic performance of a 42%-scale bridge column-to-cap beam system model, while the displacement ductility capacity was 20% lower than its CIP reference under quasi-static cyclic loading. Weinert (2011) investigated and compared different connection types for precast bridges in seismic regions, but the additional curing time of concrete to the grouted pocket connections led to the least favorable choice among the accelerated construction options. Motaref (2011) investigated the pocket connections for column-to-footing joints with a two-column bridge bent. The plastic hinge regions were enhanced with engineered cementitious composite and a concrete-filled fiber-reinforced polymer tube for each column. The connections were well protected with no damage under shake-table testing.

Member socket connections, however, retain a socket in which an entire precast member (e.g., bridge column) can be inserted and grouted. It differs from a pocket connection in that reinforcing bars are completely encased in each member, and there is no bare reinforcement that crosses the interface between the two connecting members. The connecting members are bonded by the grout and prying action. Interface surfaces are often roughened to enhance the

[1]Associate Professor, Dept. of Bridge Engineering, Tongji Univ., 1239 Siping Rd., Shanghai 200092, China. Email: wangzhiq@tongji.edu.cn

[2]Ph.D. Candidate, Dept. of Civil, Architectural and Environmental Engineering, Missouri Univ. of Science and Technology, 1401 N Pine St., Rolla, MO 65409. Email: tl9t2@mst.edu

[3]Assistant Professor, Dept. of Bridge Engineering, Tongji Univ., 1239 Siping Rd., Shanghai 200092, China (corresponding author). ORCID: https://orcid.org/0000-0001-8375-0613. Email: 86quhy@tongji.edu.cn

[4]Professor, Dept. of Bridge Engineering, Tongji Univ., 1239 Siping Rd., Shanghai 200092, China. Email: wei_hongyi@tongji.edu.cn

[5]Engineer, R & D Center for Highway Maintenance of Liaoning Traffic Planning and Design Company, Ltd., 1 Herong Rd., Shenyang 110100, China. Email: mailto:liyb_89@163.com

Note. This manuscript was submitted on February 28, 2018; approved on April 02, 2019; published online on September 5, 2019. Discussion period open until February 5, 2020; separate discussions must be submitted for individual papers. This paper is part of the ***Journal of Bridge Engineering***, © ASCE, ISSN 1084-0702.

bond resistance. The construction process is the simplest among all assembling approaches, while bond strength may not reach an equivalent level. Matsumoto (2009) and Restrepo et al. (2011) reported that the seismic behavior of the socket connection for column-to-cap joints was emulative of the CIP structures. It was confirmed by Weinert (2011) that connections can be further extended to the column-to-cap joints and pile-to-pile-cap joints, in addition to the column-to-cap joints. Khaleghi et al. (2012) studied the socket foundation that connected columns to spread footings, which showed acceptable seismic behavior. Haraldsson et al. (2013) tested three column specimens with column-to-footing socket connections. The cyclic tests showed that these specimens were comparable to the CIP reference if the column embedment length is no less than the column diameter. Belleri and Riva (2012) conducted experimental tests on connections of four precast subassemblies, and only slight strength deterioration was observed compared to the CIP specimen. White (2014) utilized the column-to-footing socket connection for a bridge substructure, and it showed promising results with slightly lower energy dissipation capabilities, but good strength and ductility. Socket connections are widely used in the building industry, but only a few studies have shown its application in bridge structures (Marsh et al. 2011).

This study presents a systematic experimental and numerical comparison of four 1/3-scale specimens of bridge columns, including two CIP references and two precast column specimens. All the specimens were tested and compared under the same quasi-static cyclic loading protocol in order to study the differences of seismic performance. The specimens were designed for the investigation and verification of actual urban viaducts in Shanghai, China (Wang et al. 2018; Qu et al. 2018), aiming to address difficulties encountered during real-world applications. More specific technical contributions with respect to each type of connection are stated as follows. For socket connection, the appropriate embedment length of longitudinal rebars and their inside diameter of bend were first designed to fully develop or anchor the desired force in the rebar. Second, the high-strength-mortar-filled shear key design between the footing and column was applied. The shear keys were able to effectively transfer forces from the column base to the footing to prevent the footing from being damaged at the bottom. After the seismic performance of shear keys was validated, they were directly applied to the pile foundation, not just the spread footing. A 0.15-m-deep groove was also cut down the bottom surface of the footing of the specimen to simulate the pile foundation. The socket connection between the column and spread footing has been intensively studied (Canha et al. 2009; Haraldsson et al. 2013; Marsh et al. 2013), but its application to a pile foundation is meager. This justifies the necessity and novelty of the current study. With respect to a pocket connection, the novelty is the implementation of corrugated steel tubes (providing lateral restraint) and higher strength concrete in the pocket. Since the embedment length of the pocket connection (27.5d, where d is the rebar diameter) is less than the requirements specified by codes for highway reinforced concrete, 30d (MOT 2004), and for seismic design of urban bridges, 40d (MOHURD 2011), in China, the use of corrugated steel tubes and higher strength concrete in the pocket can compensate for the shorter embedment length of the pocket connection and enhance its seismic performance. Each type of connection (socket and pocket) was improved by the aforementioned associated approaches and investigated experimentally and numerically to compare their seismic performance with the corresponding CIP reference column. This study builds a solid foundation for the application of socket and pocket connections to real-world precast urban viaducts. Numerical investigations were achieved by finite-element models (FEMs) that consider the features of different connection types.

Test Setup of Bridge Columns

Specimen Design and Fabrication

The specimen design (Figs. 1 and 2) was based on the actual segmental bridges of the urban viaduct in Shanghai, China. There were two testing groups, and each group consisted of one CIP reference (Specimens 1 and 3) and one precast specimen (Specimens 2 and 4). The first testing group was for the study of the seismic performance of the socket connection, while the second was for the pocket connection. All specimens were 1/3 scale, and the detailed similitudes are given in Table 1. To further explain the similitude law, three major design parameters (length, force, and moment) are provided here. The cross-sectional dimension of the prototype rectangular bridge column was 1,600 × 1,500 mm. Based on the length scale C_l of 1/3 in Table 1, the cross-sectional dimension of the column specimen was determined as 530 × 500 mm. Similarly, the diameter of the circular bridge column obeyed the same length scale (1,650 to 550 mm). The vertical loads, representing dead load from the superstructure applied on the specimens, were calculated

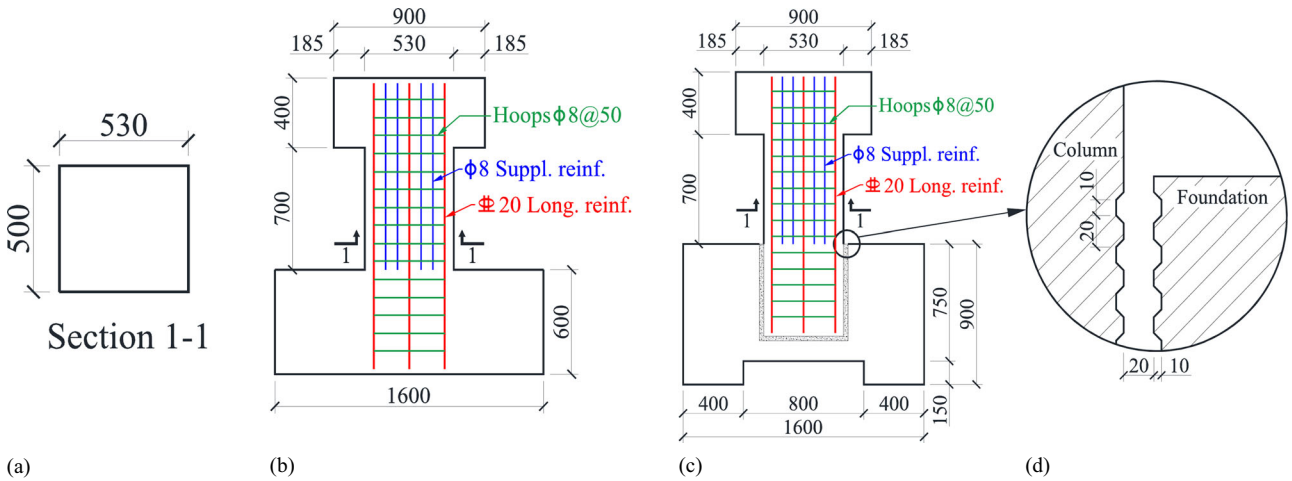

Fig. 1. (Color) Design of column specimens for socket connection comparison: (a) cross section of the column; (b) Specimen 1; (c) Specimen 2; and (d) shear key detail of Specimen 2. All dimensions are in millimeters.

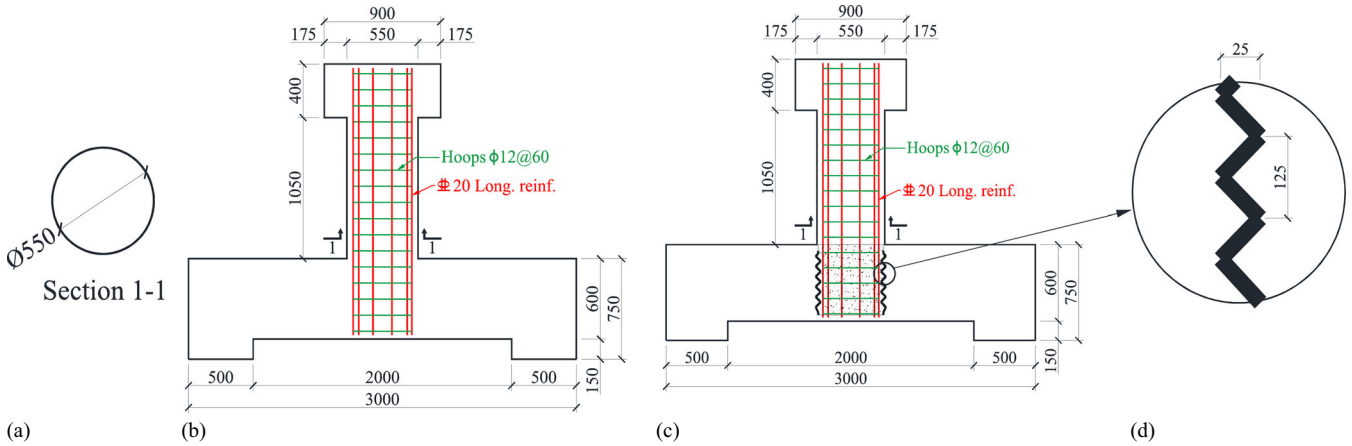

(a) (b) (c) (d)

Fig. 2. (Color) Design of column specimens for pocket connection comparison: (a) cross section of the column; (b) Specimen 3; (c) Specimen 4; and (d) steel pocket detail of Specimen 4. All dimensions are in millimeters.

Table 1. Design similitudes of the specimens

Parameter	Value
C_l	1/3
C_x	1/3
C_E	1
C_σ	1
C_ε	1
C_p	1/9
C_M	1/27
C_q	1/3
C_K	1/3

Note: l = length; x = displacement; E = elastic modulus; σ = stress; ε = strain; p = force; M = moment; q = distributed load; and K = stiffness.

based on the force scale C_p of 1/9. The actual loads of the prototype bridge were 4,692 and 4,381 kN for socket and pocket connections, respectively. The theoretical vertical loads for each corresponding column specimen were thus calculated as 521 and 487 kN. Regarding the design of longitudinal reinforcement for the rectangular bridge column, there were a total of 24 rebars with 40-mm diameters in the prototype [Fig. 3(a)]. To be more specific, the initial and effective flexural strengths of the section were 9,561 and 11,620 kN · m along the direction parallel to the 1,600-mm edge, whereas they were 8,987 and 10,990 kN · m in the other direction. According to the moment scale ($C_M = 1/27$), the initial and effective flexural strengths of the rectangular column specimen were 354 and 430 kN · m along the direction parallel to the 530-mm edge and 333 and 407 kN · m in the other direction. The main longitudinal reinforcement of the rectangular column specimen was thus determined as 10 rebars with 20-mm diameter [Fig. 3(c)]. In a similar way, the longitudinal reinforcement of the circular bridge column consisted of 24 rebars with 40-mm diameter for the prototype [Fig. 3(b)] and of 10 rebars with 20-mm diameter for the specimen [Fig. 3(d)]. Corresponding initial and effective flexural strengths were 7,317 and 9,018 kN · m for the prototype and 271 and 334 kN · m for the specimen. In addition to these three major design parameters, the same type of concrete and reinforcement were used for the column specimens as the prototype bridge.

Fig. 1 shows the designs of Specimens 1 and 2, and both shared the same cross-sectional design of the column, which was 530 × 500 × 700 mm with the mounting portion of 900 × 500 × 400 mm. The footings of the two specimens were different since Specimen 2 needed a larger space to accommodate the socket connection. Therefore, the dimension of the footing of Specimen 1 was 1,600 × 1,600 × 600 mm, while that of Specimen 2 was 1,600 × 1,600 × 900 mm. The reserved socket was 570 × 540 × 620 mm, which allowed the embedded depth of 600 mm for the column of Specimen 2 to be inserted. A 20-mm gap between the socket and the column was kept for the grouting of high-strength mortar. In addition, shear keys were implemented to the connecting surfaces of both column and footing, and the detail of the shear key is given in Fig. 1(d).

For Specimens 3 and 4 (Fig. 2), the circular columns retained a diameter of 550 mm and clear height of 1,050 mm. The mounting cap was 900 × 650 × 400 mm in dimension, and the footing was 3,000 × 750 × 600 mm. The reserved pocket within the footing of Specimen 4 was 550 mm deep and had an inner diameter of 500 mm. Corrugated steel tubes [Fig. 2(d)] were adopted to provide lateral restraint for the pocket, of which the wall thickness was 2 mm, the corrugation height was 25 mm, the corrugation interval was 125 mm, and the yield strength was 235 MPa. Different from a socket connection, there existed protruding longitudinal rebars from the lower end of the column of Specimen 4, the lengths of which were 575 mm.

The materials used were C40 and C60 concrete, high-strength grout, hot-rolled plain bars with nominal yield strength of 300 MPa (HPB300), and hot-rolled ribbed bars with nominal yield strength of 400 MPa (HRB400). The C40 concrete was used for CIP specimens and precast members, and the nominal uniaxial compressive strength of C40 was 26.8 MPa. Based on representative compression tests of 21 150-mm concrete cubes, the average values of uniaxial 28-day compressive strength of C40 was 34.8 MPa (±1.2 MPa). The C60 concrete was used for the pocket connection, and its average 28-day compressive strength was 62 MPa (±1.5 MPa). High-strength grout was used for the socket connection, and six 70-mm grout cubes were modeled and standardly cured with the average 28-day compressive strength of 69 MPa (±2.1 MPa). The moduli of elasticity of HRB400 and HPB300 were 2.0×10^5 and 2.1×10^5 MPa. The average measured yield strengths of HPB300 and HRB400 were 373.19 and 488.43 MPa based on the coupon tests of six specimens of each steel type. The average ultimate strengths were 527 and 646 MPa, respectively. The material property was determined according to the code for design of concrete structures (MOHURD 2010) for both concrete and rebar testing.

Detailed reinforcement arrangements of the columns are shown in Fig. 3. For Specimens 1 and 2 [Fig. 3(a)], the longitudinal reinforcements consisted of 20-mm-diameter HRB400s for load carrying and 8-mm-diameter supplementary HPB300s for crack prevention, while the hoops and ties were 8-mm-diameter HPB300s spaced

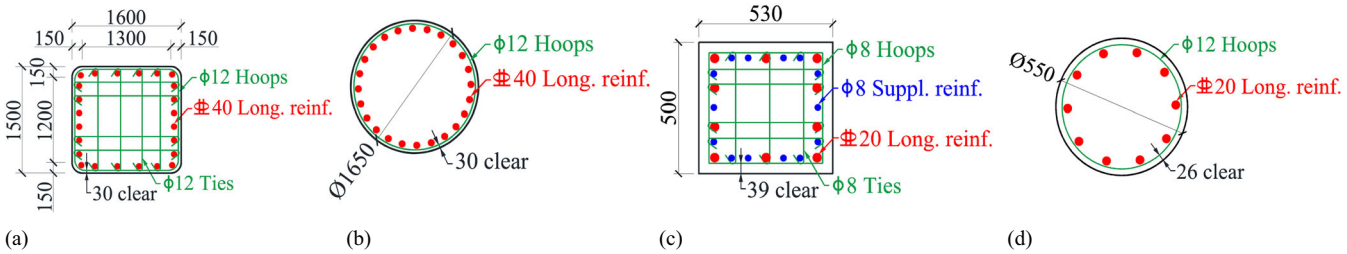

Fig. 3. (Color) Reinforcement arrangement: (a) prototype of Specimens 1 and 2; (b) prototype of Specimens 3 and 4; (c) Specimens 1 and 2; and (d) Specimens 3 and 4. All dimensions are in millimeters.

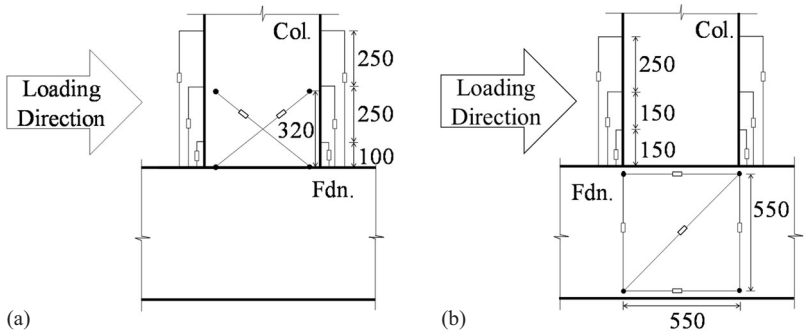

Fig. 4. Displacement sensor deployment: (a) Specimens 1 and 2; and (b) Specimens 3 and 4. All dimensions are in millimeters.

at 50 mm. The concrete cover was 39 mm thick. For Specimens 3 and 4, 20-mm-diameter HRB400s were the only longitudinal reinforcement, and they were confined by the 12-mm-diameter HRB300 circular hoops that were spaced at 60 mm. The concrete cover was thinner than Specimens 1 and 2, which was 26 mm.

Specimens 1 and 3 were the CIP structures, and they followed the conventional construction process. The precast segments of Specimens 2 and 4 included column and footing [Figs. S1(a and d)]. After the concrete was cured, the column was mounted on the footing by inserting the column to the corresponding connection locations [Figs. S1(b and e)]. A 2-cm gap between the footing and column of Specimen 2 was kept and formwork was created for grouting. By holding the columns in position, high-strength mortar was grouted into the connections until saturation was reached [Fig. S1(c)]. For Specimen 4, instead of high-strength mortar, C60 concrete was poured into the hollow section [Fig. S1(f)]. After curing (28 days), Specimen 4 was ready for testing.

The potential damages were focused at the column-to-footing region (Wang et al. 2018; Li et al. 2018), and therefore measurements for all specimens were taken at this location, including strain, displacement, and loading forces. A pair of sensors with the same height were considered as a group and mounted on two sides of the column that were perpendicular to the loading direction, and there were three groups for each column of all specimens. For Specimens 1 and 2, displacement sensors were deployed measuring relative distance changes from the column bottom to 100, 350, and 600 mm, as given in Fig. 4(a). On the other hand, sensor pairs were placed at 150, 300, and 550 mm above the column bottom for Specimens 3 and 4 [Fig. 4(b)]. Displacement sensors were also arranged to measure the displacement of the footing in order to cancel any testing errors induced by slippage. Shear deformations were captured by placing the displacement sensors on the surfaces of the columns that were parallel to the loading direction for Specimens 1 and 2 [Fig. 4(a)], while the sensors were attached to the footing instead for Specimens 3 and 4 [Fig. 4(b)] due to the circular design of the columns. Strain gauges were attached to the reinforcements of both types of specimens and the steel pocket of Specimen 4, as detailed in Fig. 5. The strain gauge model was BX120-3aa (3×2 mm) (HYCL Engineering Sensor Factory, Taizhou, China), which has a resistance of 119.9 and sensitivity of 2.060. The sampling rate of the data acquisition system was 5 Hz.

Loading Protocol

The columns were subjected to quasi-static unidirectional cyclic loading with the 1,500-kN actuator (MTS 793, MTS Systems Corporation, Eden Prairie, Minnesota), as shown in Figs. 6(a and b). The actuator had a built-in load cell and displacement sensor and was placed at the load stub of each specimen, and the maximum travel distance was ± 250 mm. The specimens were then tested with a predefined loading protocol as shown in Fig. 6(c). The specimens were also vertically loaded via hydraulic jacks to simulate the dead load from the superstructure. The actual applied vertical loads for the four specimens are given in Table 2, and the errors are within 7%. In order to keep the vertical load relatively constant, rollers were added in between the hydraulic jack and loading frame.

Experimental Results and Discussion

Damage Development and Failure Mechanism

The seismic performance of the bridge was divided into five levels (Hose and Seible 1999), including (1) cracking, (2) yielding, (3) initiation of local mechanism (e.g., plastic hinge), (4) full development of local mechanism, and (5) strength degradation. As shown in Fig. S2, each performance level of Specimen 1 was fully experienced until failure. The concrete cracks of Levels I–IV are highlighted with red curves for better clarity, and the same approach applies to the other specimens. Specimens at Level V typically experience major plastic damage, and cracks are therefore not

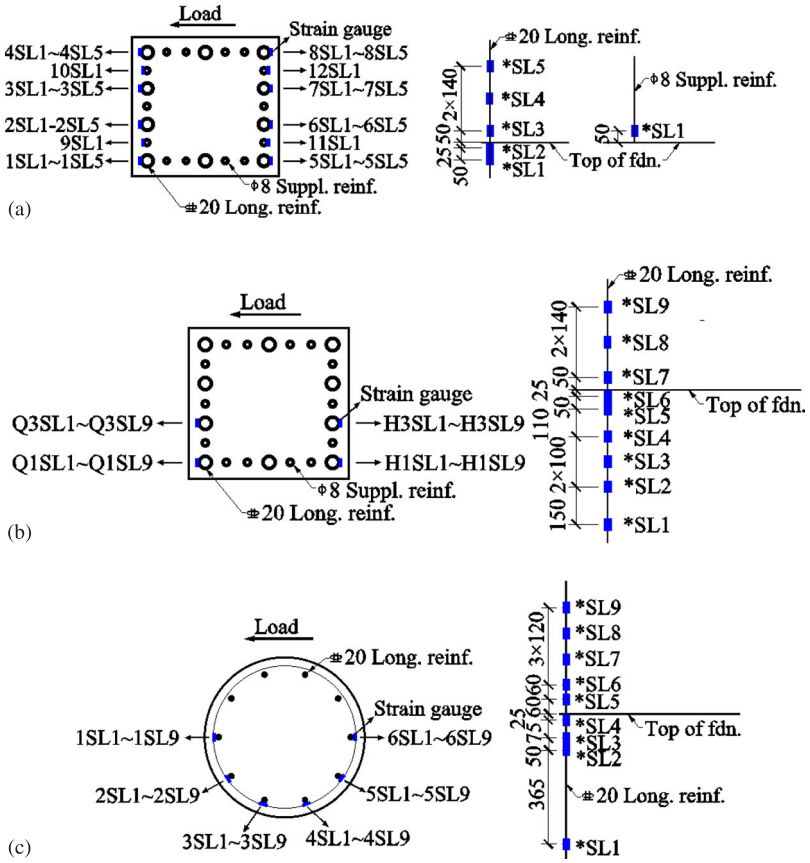

Fig. 5. (Color) Strain gauge deployment: (a) Specimen 1; (b) Specimen 2; and (c) Specimens 3 and 4. All dimensions are in millimeters. Strain gauges are numbered as *SL#, where * = number of rebars; and # = sequence of strain gauges on each rebar.

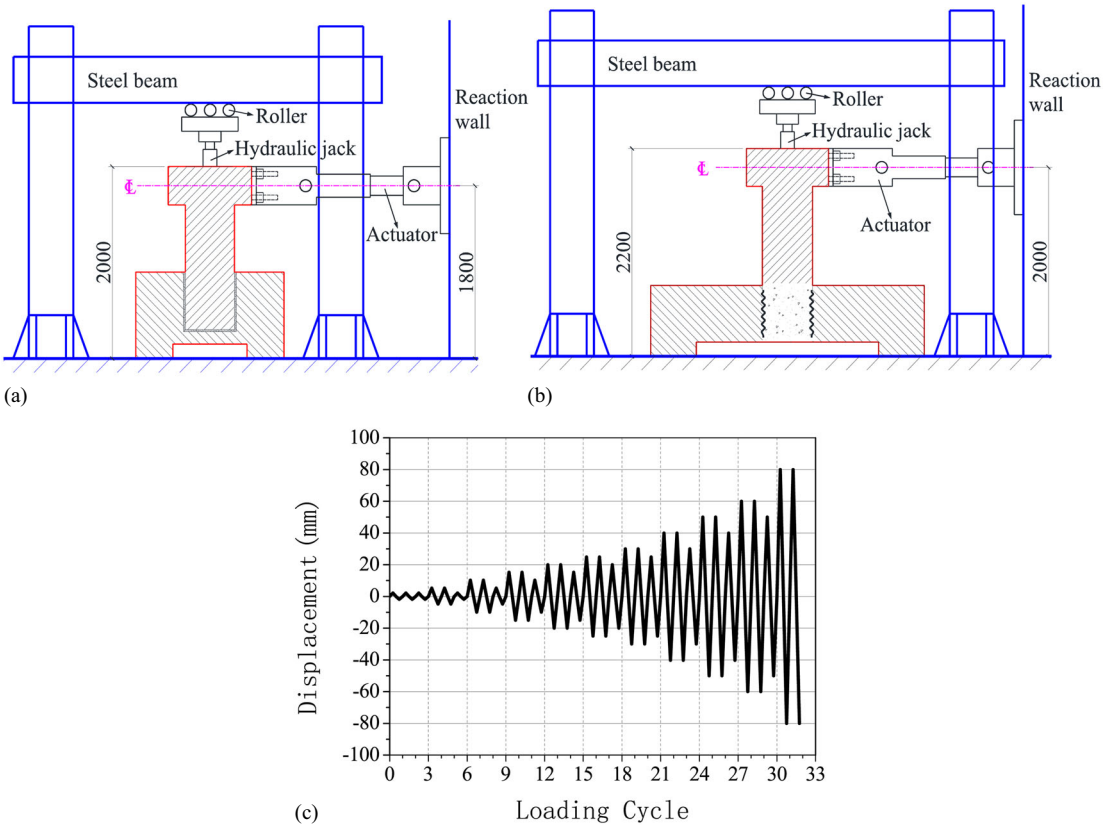

Fig. 6. (Color) Final test design: (a) test setup of Specimens 1 and 2 (dimensions in mm); (b) test setup of Specimens 3 and 4 (dimensions in mm); and (c) loading protocol.

marked. Level I started with the hairline crack at 20 cm above the column-to-footing interface, and such hairline cracks were closed when the column was recentered. When the lateral displacement of the column top reached 10 mm, the yielding of outer longitudinal rebars indicated the presence of Level II. The applied force of the actuator was 482 kN. Along with the yielding, more cracks were observed, which were generally spaced at 10 cm. At Level III, existing cracks were interconnected and widened into major ones at the column bottom regions, and a 15-cm-wide spalling region was fully developed once Level IV was reached. Finally, the buckling and fracture of several longitudinal reinforcements, together with the crushing of core concrete, marked the termination of the test, which led to Level V. The damaged region was measured at 30 cm wide. For Specimen 2 (Fig. S3), the damage development was similar to that of Specimen 1. It also reached Level II at the lateral displacement of 10 mm, while the yielding force was higher than that of Specimen 1, which was 513 kN. Major cracks that were 3 to 4 mm wide could be found at Level III, and a relatively wider plastic region was observed within 20 cm at Level IV. However, the final damage area was still within 30 cm at Level V. Only the hoops were fractured, and fracture of the longitudinal rebars was not present. Concrete crushing and reinforcement buckling were also seen at the final stage, but high-strength mortar experienced little damage.

The seismic performance levels of Specimen 3 are given in Fig. S4. Several hairline cracks were spotted at Level I, which closed up once recentered. The yielding (Level II) of the outer longitudinal reinforcement happened at the lateral displacement of 11 mm, and the corresponding lateral force imposed by the actuator was 348 kN. At Level III, the major crack between the column and footing became 1.5 mm wide. Once the plastic hinge region was fully developed at Level IV, the spalling of concrete cover was observed together with further development of the major cracks. The final failure stage was indicated by the fracture of the outer longitudinal rebars and the full spalling of concrete cover, while the damage height was approximately 25 cm above the column bottom. For Specimen 4 (Fig. S5), yielding was seen at the lateral displacement of 10 mm, when the force of the actuator reached 307 kN at Level II. The largest crack width was 3 mm at Level III, which was higher than Specimen 3 (1.5 mm). Concrete spallings were 15 and 20 cm in height for Levels IV and V, which were both less than those of Specimen 3.

Table 2. Vertical load

Specimen	Load (kN)
1 (CIP)	557
2 (socket)	531
3 (CIP)	514
4 (pocket)	520

Hysteretic Behavior and Seismic Performance Indexes

The hysteretic behaviors of Specimens 1 and 2 generated by the quasi-static cyclic tests are given in Fig. 7, and both hysteresis loops cover a good amount of area, indicating effective energy dissipation capability. The corresponding backbone curves derived from the hysteresis loops of the two specimens are shown in Fig. 7, together with five performance levels (Qu et al. 2018). The two specimens exhibited almost identical initial stiffness, while minor differences of strength were found after 10 mm of lateral displacement, where the high-strength mortar increased both the stiffness at the later stage and the ultimate strength (8% higher) for Specimen 2. The little damage that the mortar experienced through the test proves that the design of the high-strength-mortar-filled shear key is effective in maintaining structural integrity.

To better evaluate the seismic performance of the columns, further analysis was performed based on the data directly or indirectly collected via various sensors, which include strain (ε_s, curvature, drift ratio (DR), ductility (μ), residual deformation index (RDI), equivalent viscous damping ratio (ξ_{eq}), and normalized effective stiffness (K_n). To be specific, DR is defined as the ratio of the lateral displacement to the column height. Ductility, μ, is defined as the ratio of ultimate displacement (Δ_u) to effective yield displacement (Δ_y), where Δ_u is the displacement where the strength decreases to 85% of the maximum value, and Δ_y is determined by the method proposed by Park and Paulay (1990). RDI is the indicator for the assessment of the self-recovery capability of a structure. It is defined as the ratio of residual displacement to yield displacement: $\text{RDI} = \Delta_r/\Delta_y$. Stiffness degradation is analyzed through the ratio of effective stiffness (K_{eff}) to initial stiffness (K_0) at different displacement levels, namely, normalized effective stiffness (K_n). Equivalent viscous damping ratio, ξ_{eq}, is equal to $E_d/(4\pi E_s)$, where E_d is the area covered by the hysteresis loops and E_s is equivalent elastic energy ($E_s = \Delta \cdot K_{\text{eff}}$). Such damping ratio is an important index for energy dissipation capability: the higher the value, the more energy the structure dissipates.

All the indexes at five damage levels are listed in Table 3 for both Specimens 1 and 2. Ductility values were fully exploited at

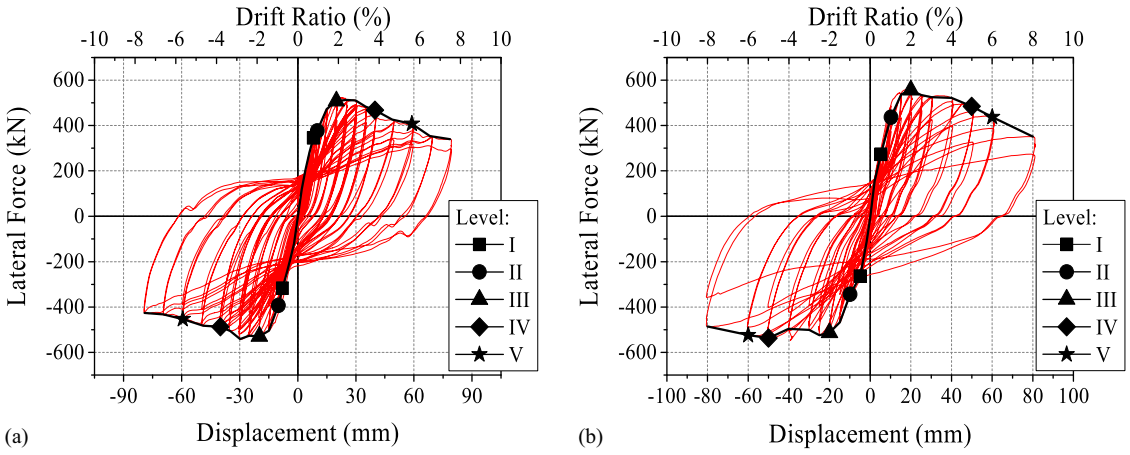

Fig. 7. (Color) Hysteretic behavior and extracted backbone curve: (a) Specimen 1; and (b) Specimen 2.

J. Bridge Eng., 2019, 24(11): 04019105

Level V for the specimens, and they were both 5.0 with the corresponding DRs of 6.11% and 6.67%, respectively. Therefore, the socket connection provides displacement capacity equivalent to the CIP column. In terms of energy dissipation and hysteretic behavior, Level IV was the most typical stage, where plastic hinges were fully developed for each specimen. Equivalent values were found for all indexes, which include ξ_{eq} (23.6% and 23.7%), RDI (2.4 and 2.61), and K_n (0.27 and 0.23). Considering every aspect of the seismic performance demonstrated by the indexes, seismic performance of the bridge column with socket connection was as good as, if not better than, the CIP column. The precast column had even better performance at certain levels (e.g., ductility at Level IV), demonstrating the robustness and feasibility of using such a connection approach.

Selected representative strain developments of the reinforcing bars are given in Figs. 8 and 9 for Specimens 1 and 2. Not all the strain gauges are shown in the figures to avoid the confusion of having too many curves. It can be observed that yielding of rebars typically initiated at higher locations above the interface (>50 mm above the interface), while the rebars within the foundation generally experienced little damage until the ultimate strength (around 30 mm of lateral displacement) was reached. The yielding process of rebars in Specimen 2 started as early as the displacement level of 10 mm, and most of the rebar damages came from above the foundation within the displacement level of 30 mm. After that, it started to penetrate to deeper locations, but little damage was found beyond the depth of 250 mm below the interface throughout the testing procedure, indicating good structural integrity.

The hysteretic behavior and extracted backbone curves of Specimens 3 and 4 are respectively shown in Fig. 10(a and b). Both the yielding strength (307 kN) and failure strength (254 kN) of Specimen 4 were less than the CIP reference column (348 and 305 kN), although the corresponding displacement values were similar. The ultimate strengths at Level III for Specimens 3 and 4 were 329 and 378 kN, which again confirms that the strength of the precast Specimen 4 was consistently lower. This was largely due to the lack of reinforcements provided by the footing within the pocket connection.

Indexes were also utilized to facilitate the comparison of Specimens 3 and 4 for better evaluation of the seismic performance of a pocket connection (Table 4). Ductility of Specimen 4 was higher than that of the CIP Specimen 3 at almost all levels, and the difference became more significant when the loading level progressed. The corresponding DR values of Specimen 4 were thus higher than those of Specimen 3. Although the strength values were less for

Table 3. Comparison of seismic performance indexes for Specimens 1 and 2

	ε_s		DR (%)		μ		RDI		ξ_{eq} (%)		K_n	
Level	1	2	1	2	1	2	1	2	1	2	1	2
I	$<\varepsilon_y$	$<\varepsilon_y$	0.90	0.58	0.7	0.4	0.18	0.18	5.8	9.9	0.99	1.21
II	$=\varepsilon_y$	$=\varepsilon_y$	1.03	1.13	0.8	0.9	0.27	0.26	6.9	8.8	0.95	0.99
III	0.030	0.024	2.22	2.22	1.8	1.7	0.75	0.58	12.8	11.9	0.59	0.65
IV	0.030	0.031	4.43	5.55	3.6	4.2	2.40	2.61	23.6	23.7	0.27	0.23
V	—	0.031	6.11	6.67	5.0	5.0	—	3.44	—	26.6	—	0.17

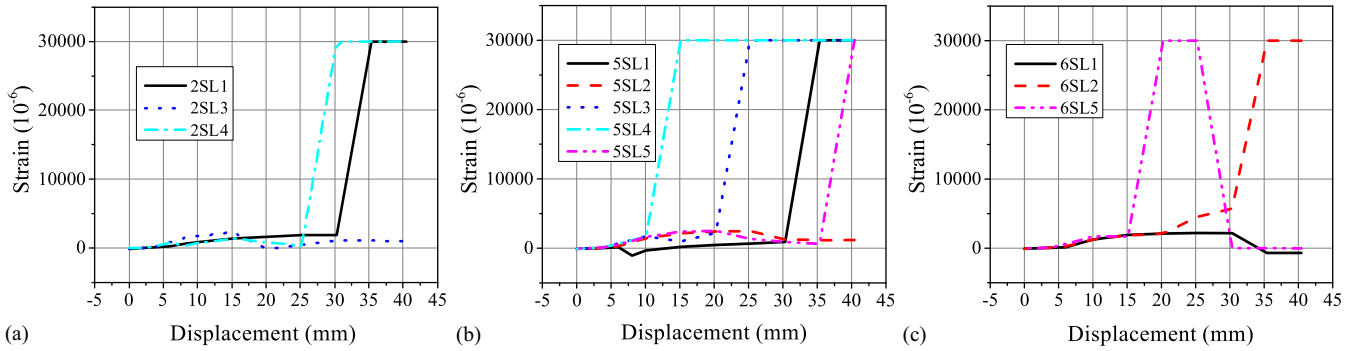

Fig. 8. (Color) Selected strain development of rebars from Specimen 1: (a) 2SL#; (b) 5SL#; and (c) 6SL#.

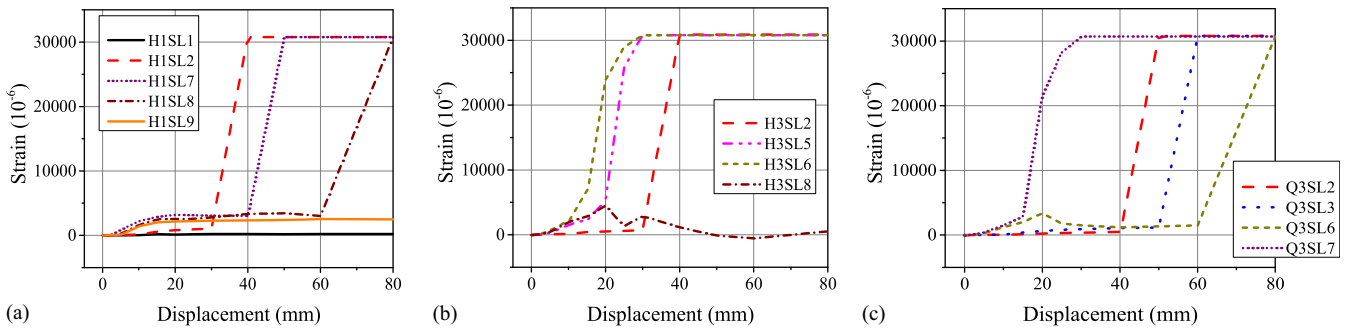

Fig. 9. (Color) Selected strain development of rebars from Specimen 2: (a) H1SL#; (b) H3SL#; and (c) Q3SL#.

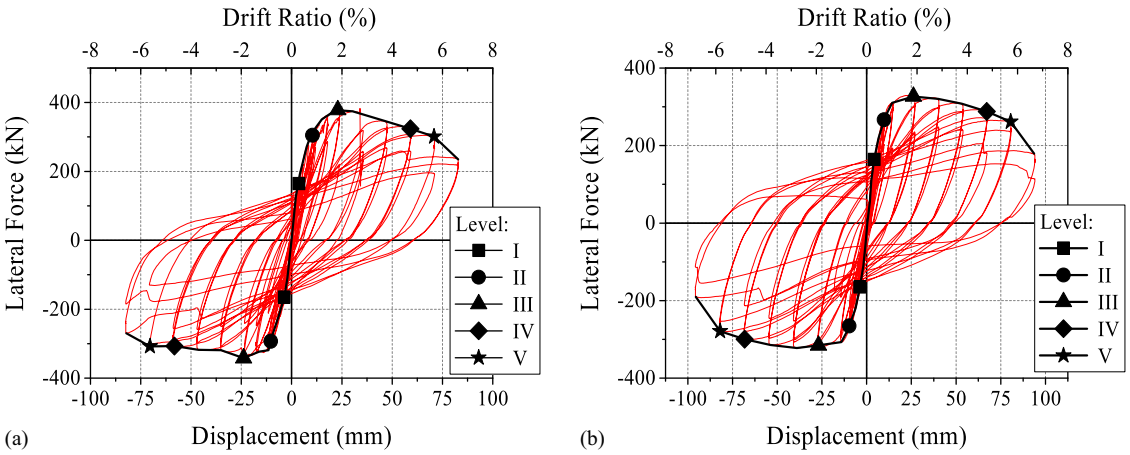

Fig. 10. (Color) Hysteretic behavior and extracted backbone curve: (a) Specimen 3; and (b) Specimen 4.

Table 4. Comparison of seismic performance indexes for Specimens 3 and 4

	ε_s		DR (%)		μ		RDI		ξ_{eq} (%)		K_n	
Level	3	4	3	4	3	4	3	4	3	4	3	4
I	$<\varepsilon_y$	$<\varepsilon_y$	0.40	0.47	0.3	0.4	0.09	0.15	9.3	7.0	1.54	1.41
II	$=\varepsilon_y$	$=\varepsilon_y$	1.15	1.08	0.9	0.8	0.14	0.18	8.8	6.1	1.00	1.00
III	0.018	0.025	2.64	2.99	2.0	2.3	0.65	1.12	14.2	20.1	0.50	0.41
IV	0.031	0.031	6.57	7.48	5.0	5.6	3.20	4.27	25.2	31.4	0.19	0.14
V	0.031	—	7.87	8.97	5.9	6.8	4.18	5.42	28.0	33.9	0.14	0.11

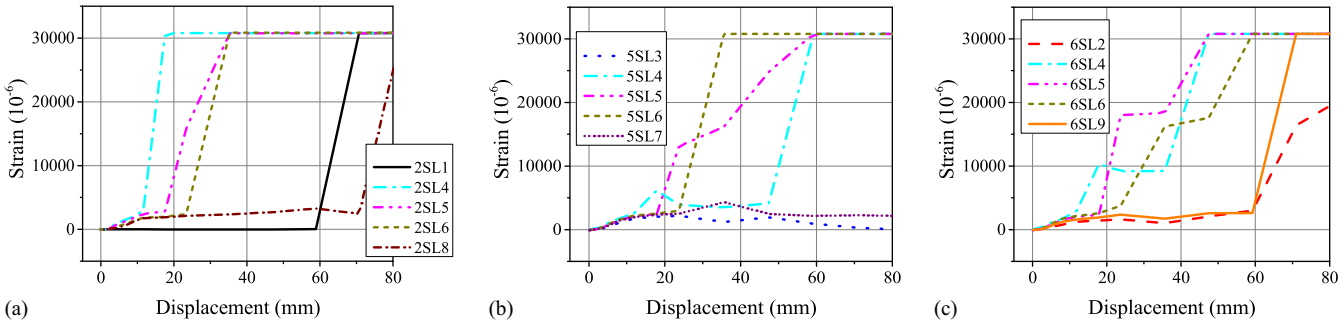

Fig. 11. (Color) Selected strain development of rebars from Specimen 3: (a) 2SL#; (b) 5SL#; and (c) 6SL#.

Specimen 4, the degradation of the strength was slower, covering an even larger area for each loop. Thus, ξ_{eq} of Specimen 4 was higher at later performance levels (III, IV, and V), indicating better energy dissipation capacity. However, the RDI of Specimen 4 was also higher than Specimen 3, and therefore the former possessed less self-centering capabilities. This is again because of less reinforcement at the connection region compared with the CIP structure, and hence less stiffness.

Strain developments of the rebars from Specimens 3 and 4 measured from the embedded strain gauges are shown in Figs. 11 and 12. The major rebar damages were within the range of 15 cm above and 5 cm below the column-to-footing interface prior to displacement Level IV. To be specific, the strain values were generally smaller in the footing, and no yielding occurred. The use of C60 concrete indeed compensated the loss of the reinforcement of footing, which secured the rebar from being extensively damaged. In addition, the corrugated pocket also experienced moderate strain variation, which was less than 1,000 με. For all Specimens 1–4, yielding penetrations were found propagating into the footing, which typically stay within 20 cm.

Numerical Simulations and Results

Finite-Element Model

FEMs were established and calibrated with DIANA. The displacement-based algorithm helps better solve the nonlinear behavior of reinforced concrete with the introduction of embedded reinforcement element (ERE) and its bond-slip behavior. Concrete material was modeled with the CHX60-BRICK solid element, which incorporates compression, tension, and cracking behaviors. The compressive behavior of concrete was based on the Mander model. Confined and unconfined models were used for core concrete and concrete cover, respectively. The parameters were determined based on the compression tests of concrete

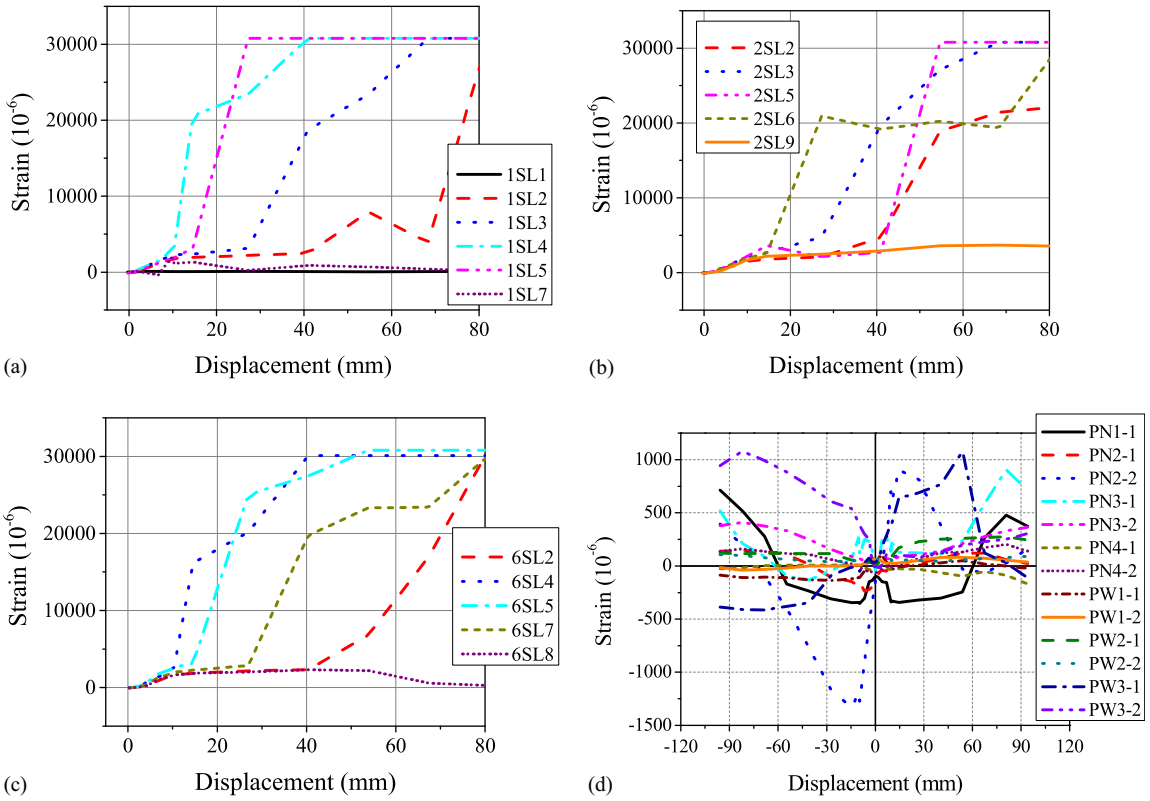

Fig. 12. (Color) Selected strain development of rebars from Specimen 4: (a) 1SL#; (b) 2SL#; (c) 6SL#; and (d) pocket.

cubes. Concrete cracking was considered by the assumption proposed by Vecchio and Collins (1993), and the reduction factor was calibrated to be 0.15 for columns with an aspect ratio of 1.7 or less. A default value of 0 is suitable for columns with an aspect ratio of 2.4 or higher. The tension softening process was simulated with the exponential curve defined in DIANA, and the fracture energy was calculated based on the CEB-FIP Model Code 1990 (CEB 1993)

$$G_f^I = G_{f0}\left(\frac{f_{cm}}{f_{cm0}}\right)^{0.7} \tag{1}$$

$$f_{cm} = f_{ck} + \Delta f \tag{2}$$

where $f_{cm0} = 10$ MPa; $\Delta f = 8$ MPa; $f_{ck} = 40$ MPa is the compressive strength of concrete; and $G_{f0} = 0.03$ is obtained based on the diameter of aggregate (16 mm).

The stress-strain relationship of the reinforcing steel was modeled with a multilinear curve to best match the test result (Fig. S6). The von Mises yield condition was employed on the yielding process of the steel based on the strain-hardening hypothesis. The material property was integrated into the ERE.

For precast specimens, connections have to be considered for potential opening or crushing behaviors. The precast members of Specimen 2 were directly connected with high-strength mortar, which was simulated by the CHX60-BRICK element with the tested strength. For the connection region of Specimen 4, the mortar was modeled by the same element, and the material property was based on the compression test of C60 concrete. The steel pocket boundary was simulated with the shell element. Plane interface element CQ48I, which considers discrete cracking, was used to model connection behavior, for example, openings at the interface.

Model Validation

The CIP Specimen 1 utilized the CHX60-BRICK and ERE for concrete and reinforcement modeling as detailed in the previous section, while the mounting cap simply used elastic concrete material. The numerical model of Specimen 1 is shown in Fig. 13. Vertical load was applied with uniformly distributed force, while the lateral load was concentrated at the actual loading point. The optimal mesh size of the solid elements was 50 mm, and the bottom of the footing was fixed.

Due to the material nonlinearity and mesh complexity, monotonic pushover analysis was performed instead of the actual cyclic loading, and the numerical result was then compared with the backbone curve of the test. As shown in Fig. 14(a), the initial stiffness, ultimate strength, and degradation trend can be effectively matched with the test results. To be specific, the difference of the ultimate strength between the numerical result (525 kN) and the test result (513 kN) was only 2.3%. The integration of cracking and strength degradation within the reinforced concrete materials in the FEMs was able to simulate such a decrease in the actual column with good convergence.

The stress distribution and crack pattern at each performance level are given in Figs. S7 and S8. With the increase of the lateral displacement, the major compressive region was expanded from a corner to the loading point via a diagonal line across the column. Such diagonal line started to appear at the displacement level of 25 mm and was fully developed at 55 mm. Together with the expansion of the compressive regions, the gradually increased cracking and crushing of concrete resulted in the decrease of the total compressive strength of the column. The height of the concrete crushing region was found to be 30 cm in the simulation, which agrees with the test result.

Specimen 2 was modeled using the same approach as Specimen 1, while the connection was simulated with high-strength mortar. The numerical model of Specimen 2 is shown in Fig. 15. Again,

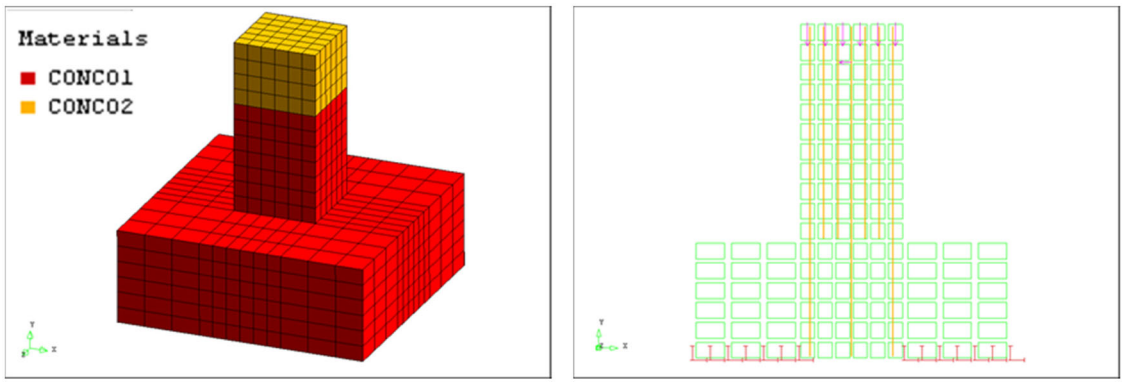

Fig. 13. (Color) Numerical model of Specimen 1: (a) concrete material definition; and (b) reinforcement arrangement and boundary condition.

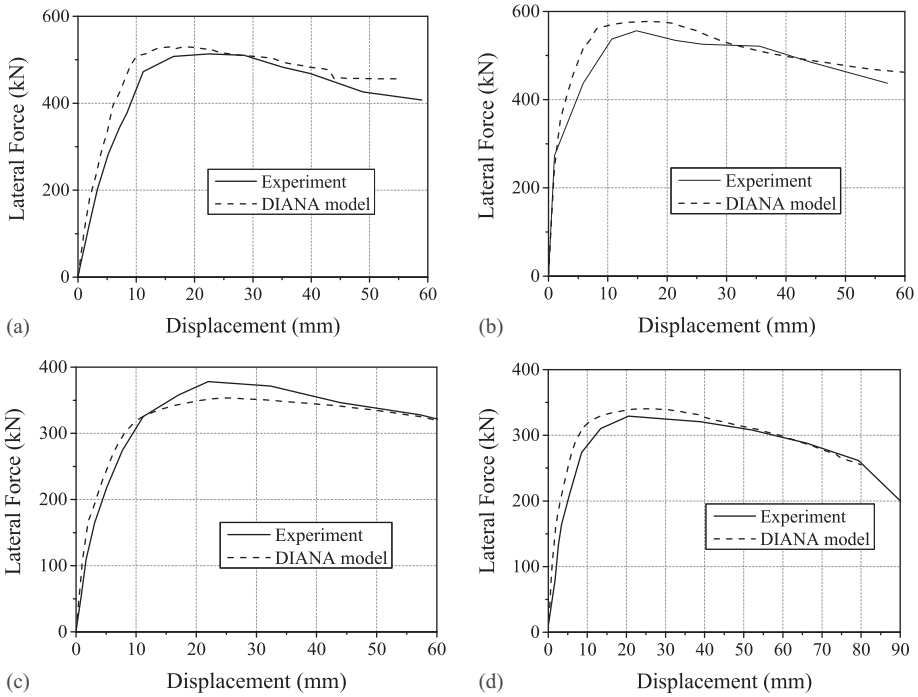

Fig. 14. Comparison of experimental and numerical results: (a) Specimen 1; (b) Specimen 2; (c) Specimen 3; and (d) Specimen 4.

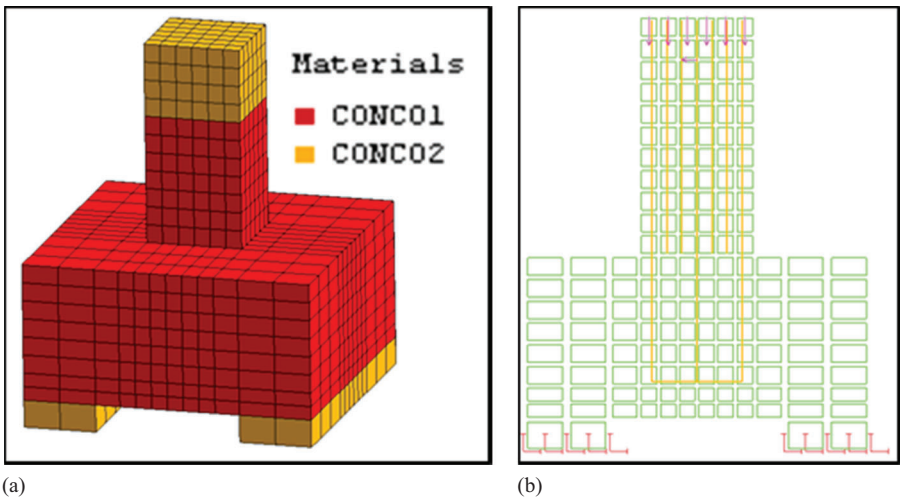

Fig. 15. (Color) Numerical model of Specimen 2: (a) concrete material definition; and (b) reinforcement arrangement and boundary condition.

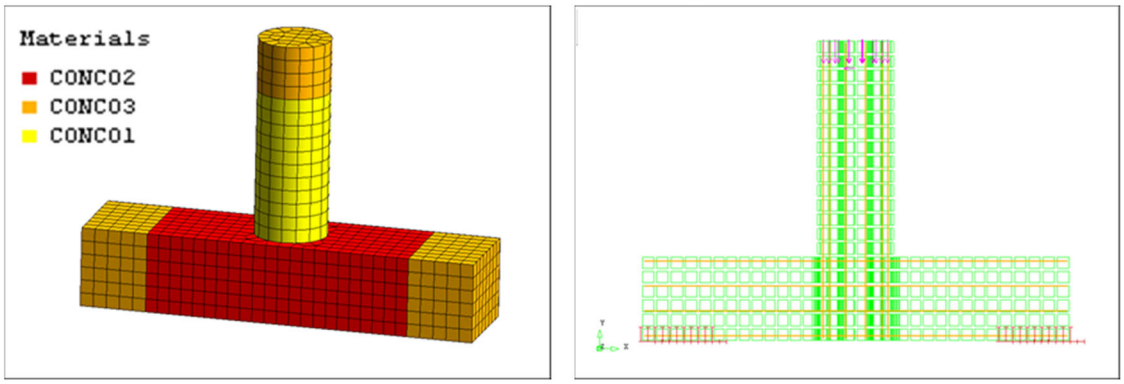

(a) (b)

Fig. 16. (Color) Numerical model of Specimen 3: (a) concrete material definition; and (b) reinforcement arrangement and boundary condition.

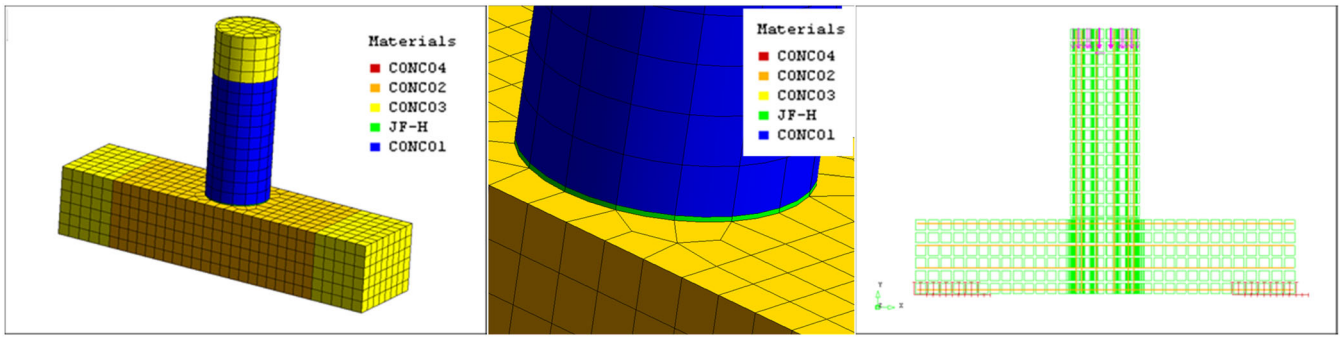

(a) (b) (c)

Fig. 17. (Color) Numerical model of Specimen 4: (a) concrete material definition; (b) detail of interface element; and (c) reinforcement arrangement and boundary condition.

good agreement was found between the numerical and test results [Fig. 14(b)]. The difference of the ultimate strength was 3.5%, and major discrepancy existed around the lateral displacement of 5 mm where initial yielding was encountered.

Since the high-strength grout was able to sustain high compressive strength, little damage was experienced for both the experimental and simulated columns. Therefore, damages were still localized at the bottom region of the column, and the development of the column damage of Specimen 2 (Figs. S9 and S10) was similar to Specimen 1. The crushing height of the concrete also agreed well with the test result, which was around 35 cm.

The modeling approach of Specimen 3 (Fig. 16) was the same as Specimen 1 with different dimensions. The entire specimen was fixed via the two ends of the footing, which matched the actual mounting situation. Such simulation approach also gave good agreement between the experimental and numerical results, as shown in Fig. 14(c).

The stress and damage development of Specimen 3 are shown in Figs. S11 and S12. The compressive stress spread over the column from the corner, while the cracking progressed from the tensioning side of the column as the load increased. Minor cracks were also present at the connection region of the footing with little increase at later stages, which agreed with the test results. The concrete crushing height was between 30 and 40 cm, which overestimated the test result (25–30 cm).

The precast segments of Specimen 4 were modeled using the same material and element as Specimen 3, while the connection region utilized the material property of C60 concrete to be consistent with the actual test specimen (Fig. 17). Since openings and closings of the column-to-footing interface were found at the connection region, interface element CQ48I was used to simulate the interface behavior. The pushover result was compared with the backbone curve of the test, as given in Fig. 14(d), where good agreements were obtained.

The stress and damage progression of Specimen 4 are shown in Figs. S13 and S14. The major trend of the stress and damage development was similar to Specimen 3, but several differences were found at later stages. First, the area of cracking within the footing was less for Specimen 4. Cracking of Specimen 4 was more concentrated at the tension side of the column, which was reflected by the opening strain obtained from both models. Moreover, the crushing height of the concrete was much less for Specimen 4, which was within 20 cm. These were also major differences found in the test results, which demonstrates the accuracy and effectiveness of the numerical model.

Conclusions

The 1/3-scale precast bridge columns with socket and pocket connections were studied both experimentally and numerically in order to perform the investigation and to verify the actual precast bridge designs of urban viaducts in Shanghai, China. Each precast column was compared with a CIP reference, and both were tested under the same quasi-static cyclic loading.

Based on the comparison of Specimens 1 and 2, the damage development and failure mechanism were similar for the precast column with socket connection and its CIP reference. The hysteretic behaviors and the derived performance indexes of the two speci-

mens were equivalent (<10% difference). It was shown that the socket connection has the same, if not a better than, level of seismic performance as the CIP construction by using the high-strength-mortar-filled shear key connection design.

For pocket connection, similar seismic performances were also found for Specimens 3 and 4. In terms of structural damage, rebar fracture and concrete crushing were found for both specimens, and minor damage (hairline cracks) occurred at the footings. Specimen 4 with pocket connection had a larger opening at the column-to-footing interface, and the plastic region was thus more concentrated due to the lack of reinforcement within the pocket region. From the comparison, the pocket connection had good seismic performance, while additional measures may be taken for strength enhancement.

DIANA can effectively simulate the damage development (e.g., concrete cracking and crushing, stiffness softening, strength degradation, and reinforcement yielding) of the CIP and precast columns. The numerical models were generally in good agreement with the backbone curves of test results, but higher initial stiffness was found due to the lack of fatigue effect from the monotonic pushover.

Acknowledgments

Financial support for this study was provided by the National Natural Science Foundation of China under Award No. 51778470.

Supplemental Data

Figs. S1–S14 are available online in the ASCE Library (www.ascelibrary.org).

References

Belleri, A., and P. Riva. 2012. "Seismic performance and retrofit of precast concrete grouted sleeve connections." *PCI J* 57 (1): 97–109. https://doi.org/10.15554/pcij.01012012.97.109.

Brunesi, E., R. Nascimbene, M. Deyanova, C. Pagani, and S. Zambelli. 2015. "Numerical simulation of hollow steel profiles for lightweight concrete sandwich panels." *Comput. Concr.* 15 (6): 951–972. https://doi.org/10.12989/cac.2015.15.6.951.

Bu, Z.-Y., Y.-C. Ou, J.-W. Song, N.-S. Zhang, and G. C. Lee. 2016. "Cyclic loading test of unbonded and bonded posttensioned precast segmental bridge columns with circular section." *J. Bridge Eng.* 21 (2): 04015043. https://doi.org/10.1061/(ASCE)BE.1943-5592.0000807.

Canha, R. M. F., E. B. Ebeling, A. L. H. de Cresce El Debs, and M. K. El Debs. 2009. "Analysing the base of precast column in socket foundations with smooth interfaces." *Mater. Struct.* 42 (6): 725–737. https://doi.org/10.1617/s11527-008-9416-4.

CEB (Comité Euro-International du Béton). 1993. *CEB-FIP model code 1990: Design code*. London: Thomas Telford.

Haraldsson, O. S., T. M. Janes, M. O. Eberhard, and J. F. Stanton. 2013. "Seismic resistance of socket connection between footing and precast column." *J. Bridge Eng.* 18 (9): 910–919. https://doi.org/10.1061/(ASCE)BE.1943-5592.0000413.

Hose, Y. D., and F. Seible. 1999. *Performance evaluation database for concrete bridge components and systems under simulated seismic loads*. PEER Rep. 1999/11. Berkeley, CA: Pacific Earthquake Engineering Research Center.

Ichinose, T., Y. Kanayama, Y. Inoue, and J. E. Bolander Jr. 2004. "Size effect on bond strength of deformed bars." *Constr. Build. Mater.* 18 (7): 549–558. https://doi.org/10.1016/j.conbuildmat.2004.03.014.

Khaleghi, B., E. Schultz, S. Seguirant, L. Marsh, O. Haraldsson, M. Eberhard, and J. Stanton. 2012. "Accelerated bridge construction in Washington State: From research to practice." *PCI J* 57 (4): 34–49. https://doi.org/10.15554/pcij.09012012.34.49.

Li, T., H. Qu, Z. Wang, H. Wei, and S. Jiang. 2018. "Seismic performance of precast concrete bridge columns with quasi-static cyclic shear test for high seismic zones." *Eng. Struct.* 166: 441–453. https://doi.org/10.1016/j.engstruct.2018.03.086.

Marsh, M. L., S. J. Stringer, J. F. Stanton, M. O. Eberhard, O. S. Haraldsson, H. V. Tran, B. Khaleghi, E. Schultz, and S. Seguirant. 2013. *Precast bent system for high seismic regions.* Rep. No. FHWA-HIF-13-037. Washington, DC: Federal Highway Administration.

Marsh, M. L., M. Wernli, B. E. Garrett, J. F. Stanton, M. O. Eberhard, and M. D. Weinert. 2011. *Application of accelerated bridge construction 25 connections in moderate-to-high seismic regions.* Rep. No. 698. Washington, DC: National Cooperative Highway Research Program.

Matsumoto, E. 2009. *Emulative precast bent cap connections for seismic regions: Grouted duct and cap pocket test results, design and construction specifications, design examples, and connection details*. ECS Rep. No. ECS-CSUS-2009-05. Sacramento, CA: California State Univ.

MOHURD (Ministry of Housing and Urban-Rural Development of the People's Republic of China). 2010. *Code for design of concrete structures*. GB 50010. Beijing: MOHURD.

MOHURD (Ministry of Housing and Urban-Rural Development of the People's Republic of China). 2011. *Code for seismic design of urban bridges*. CJJ 166. Beijing: MOHURD.

MOT (Ministry of Transport of the People's Republic of China). 2004. *Code for design of highway reinforced concrete and prestressed concrete bridges and culverts*. JTG D62. MOT.

Motaref, S. 2011. *Seismic response of precast bridge columns with energy dissipating joints*. Ph.D. thesis, Dept. of Civil and Environmental Engineering, Univ. of Nevada.

Murcia-Delso, J., A. Stavridis, and P. B. Shing. 2013. "Bond strength and cyclic bond deterioration of large-diameter bars." *ACI Struct. J.* 110 (4): 659–670. https://doi.org/10.14359/51685751.

Ou, Y.-C. 2007. "*Precast segmental post-tensioned concrete bridge columns for seismic regions*." Ph.D. thesis, Dept. of Civil, Structural, and Environmental Engineering, State Univ. of New York at Buffalo.

Park, R. J. T., and T. Paulay. 1990. "Strength and ductility of concrete substructures of bridges." *Transit N. Z. Road Res. Unit Bull.* 84: 1–14.

Qu, H., T. Li, Z. Wang, H. Wei, J. Shen, and H. Wang. 2018. "Investigation and verification on seismic behavior of precast concrete frame piers used in real bridge structures: Experimental and numerical study." *Eng. Struct.* 154: 1–9. https://doi.org/10.1016/j.engstruct.2017.10.069.

Raynor, D. J., D. E. Lehman, and J. F. Stanton. 2002. "Bond-slip response of reinforcing bars grouted in ducts." *Struct. J.* 99 (5): 568–576. https://doi.org/10.14359/12296.

Restrepo, J. I., M. J. Tobolski, and E. E. Matsumoto. 2011. *Development of a precast bent cap system for seismic regions*. NCHRP Rep. 681. Washington, DC: Transportation Research Board.

Steuck, K. P., M. O. Eberhard, and J. F. Stanton. 2009. "Anchorage of large-diameter reinforcing bars in ducts." *ACI Struct. J.* 106 (4): 506–513. https://doi.org/10.14359/56616.

Vecchio, F. J., and M. P. Collins. 1993. "Compression response of cracked reinforced concrete." *J. Struct. Eng.* 119 (12): 3590–3610. https://doi.org/10.1061/(ASCE)0733-9445(1993)119:12(3590).

Wang, Z., H. Qu, T. Li, H. Wei, H. Wang, H. Duan, and H. Jiang. 2018. "Quasi-static cyclic tests of precast bridge columns with different connection details for high seismic zones." *Eng. Struct.* 158: 13–27. https://doi.org/10.1016/j.engstruct.2017.12.035.

Weinert, M. D. 2011. *Application of accelerated bridge construction connections in moderate-to-high seismic regions*. Rep. No. 698. Washington, DC: National Cooperative Highway Research Program, Transportation Research Board.

White, S. L. 2014. "*Controlled damage rocking systems for accelerated bridge construction*." Master's thesis, Dept. of Civil and Natural Resource Engineering, Univ. of Canterbury.

Zhou, Y., Y.-C. Ou, G. C. Lee, and J. S. O'Connor. 2010. "Mechanical and low-cycle fatigue behavior of stainless reinforcing steel for earthquake engineering applications." *Earthq. Eng. Eng. Vib.* 9 (3): 449–457. https://doi.org/10.1007/s11803-010-0028-y.